JOURNAL OF COMPUTATIONAL PHYSICS **144,** 379–401 (1998)
ARTICLE NO. CP986016

Solving the Navier–Stokes Systems with Weak Viscosity and Strong Heat Conduction Using the Flux-Corrected Transport Technique and the Alternating-Directional Explicit Method

Liqun Zhou, Vincent B. Wickwar, and Robert W. Schunk

Center for Atmospheric and Space Sciences, Utah State University, Logan, Utah 84322-4405
E-mail: wickwar@aeronomy.cass.usu.edu

Received April 22, 1997; revised March 27, 1998

The flux-corrected transport (FCT) technique and the alternating-direction explicit (ADE) method are coupled through a time-splitting technique. This new combination of both methods has been used successfully to solve the fully coupled Navier–Stokes system applied to ionospheric thermal plasma flows with a viscosity and strong heat conduction. The combined scheme gives convergent solutions within the time step set for nonlinear stability of the corresponding nondissipative flow fields, and the time-dependent solutions are consistent with other model results using different methods. To have a quantitative view of the flux-limiter of Boris' FCT version, a concept of local variation is defined to identify local extrema. The total variation diminishing scheme finds unique entropy solutions for vanishing dissipation. The ADE scheme, however, enables us to handle dissipation when the FCT technique alone can be inappropriate.

1. INTRODUCTION

The flux-corrected transport (FCT) technique, developed by Boris and Book [1], solves nonlinear hyperbolic conservation laws with an explicit implementation, a primitive variable approach, a second-order accuracy in a smooth domain, and a high resolution in shocks and contact discontinuities. Based on the merits of this scheme, it is widely used in space physics research, particularly in modeling the earth's ionospheric thermal plasma flows.

In the upper atmosphere, solar extreme ultraviolet (EUV) radiation ionizes various neutral constituents, producing ion and electron pairs and forming the ionosphere. At low altitudes ($\leq$150 km), the plasma concentrations are mainly determined by local photochemical

0021-9991/98 $25.00

TABLE I
Dynamic Range of Plasma and Neutral Parameters at Mid-Latitudes

Parameter	*E* Region	*F* region peak	Plasmasphere
Ion species	NO^+, O_2^+, N_2^+	O^+	H^+, He^+
Neutral species	N_2, O_2	O	H, He
$n_e(cm^{-3})$	10^2–10^5	10^4–10^6	10^2–10^4
$n_n(cm^{-3})$	5×10^{-11}	10^9	10^5
$T_e(K)$	10^2–10^3	10^3	10^3–10^4
$T_i(K)$	10^2–10^3	10^3	10^3–5×10^3
$T_n(K)$	10^2–10^3	5×10^2–10^3	5×10^2–2×10^3
Electron heat flux (eV cm^{-2} s^{-1})	10^5–10^{10}	10^5–10^{11}	10^5–10^{11}
Exchange flux (cm^{-2} s^{-1})	0	-10^8–10^8	-10^8–10^8
Plasma condition	Weakly ionized	Partially ionized	Fully ionized

reactions, but as height increases, transport becomes dominant. Since the gyro-frequencies of the charged particles are much larger than the interparticle collision frequencies, the different ion and electron species are confined to flow along the geomagnetic field. The flowing plasma undergoes photochemical reactions, charge exchanges, particle interactions, as well as external heating and cooling processes. As a result of charge exchange and transport, the plasmasphere is formed, which extends to several earth radii along dipole-like geomagnetic field lines. Despite the different names, the ionosphere and plasmasphere are essentially composed of plasma that originates in the earth's upper atmosphere. Formulations regarding the basic physics, chemistry, and transport processes that are relevant to the ionosphere and plasmasphere are given, for example, by Schunk [2].

In general, characteristic distributions of the thermal plasma are functions of latitude, longitude, altitude, and solar zenith angle. To give some general concept about the plasma and neutral parameters at mid-latitudes, we list these in Table I for the ionospheric *E* region (100–150 km), the *F* region (150–1000 km), and the plasmasphere (above 1000 km along dipole field lines). The range of values is to account for hour-to-hour, season-to-season, and year-to-year variabilities.

During the last 20 years, there were several attempts at modeling the nonlinear transport features of ionospheric plasma flows. In modeling the poststorm plasmaspheric refilling process, the FCT technique was used to solve the coupled continuity and momentum equations of the hyperbolic type [3]. Shock waves were found during the initial transient process of replenishing an empty magnetic flux tube. The FCT technique was also used to model supersonic thermal plasma flows, as in the polar wind [4]. However, these solutions were based on inviscid flow assumptions and simplified energy conservation laws. Although the FCT technique can be conveniently applied to model some ionospheric reactive plasma flows, it was, however, originally designed for solving hyperbolic systems. This limits its direct application in modeling ionospheric plasma transport due to the existence of viscosity and nonlinear heat conduction, which are hard to handle with an explicit hyperbolic solver. Other high-resolution methods, like the Godunov method with an approximate Riemann solver, were also used in numerical simulations of thermal plasma flows in space physics [5]. However, the Godunov method requires extra manipulations at each time step on eigenvalue problems, which is time consuming. In addition, this method was also designed for idealized hyperbolic systems.

Since heat conduction is of particular importance in the ionosphere and plasmasphere, it should be solved simultaneously with the other transport processes for time-dependent simulations. Under normal situations, viscous effects may not be important, but they tend to increase with altitude and counteract discontinuities arising from nonlinear convection. Based on these considerations, we choose the Navier–Stokes systems derived from Schunk's 13-moment equations [2] as our mathematical model and seek methods to find simultaneous solutions of mixed hyperbolic and parabolic types of continuity, momentum, and energy equations. Since the FCT technique can handle nonlinear convection and reacting sources, our interest is to extend its capability by coupling it to other methods so that dissipation can be included. In addition, considering the explicit nature of FCT, another explicit scheme is desirable. It turns out that the alternating-direction explicit (ADE) method developed by Barakat and Clark [6] is particularly convenient for our systems of equations.

We first introduce our systems of conservation laws. Then, we look into the FCT and the ADE schemes. Next, we illustrate the way we couple the two schemes to solve systems of the mixed type, and we also apply the numerical technique to a specific space physics problem. Finally, the results we obtain using an FCT-ADE technique are compared to those obtained with a widely used completely implicit method.

2. EQUATIONS

The Navier–Stokes equations for multispecies thermal plasma flows can be derived by truncating the 13-moment transport equations [2]. For plasma flow along a diverging magnetic flux tube, the truncated system of continuity, momentum, and energy equations becomes

$$\bar{n}_t = -(\bar{n}u)_x + A\alpha - \beta\bar{n} \tag{1}$$

$$(\bar{n}u)_t = -(\bar{n}uu)_x + \left\{\frac{\eta}{m}\left[\frac{4}{3}(Au)_x - 2uA_x\right]\right\}_x - \frac{A}{m}p_x + \frac{e\bar{n}}{m}E + g(\mathbf{r})\bar{n} + \sum_k \nu_k \Phi_k (u_k - u)\bar{n} \tag{2}$$

$$\bar{p}_t = -(\bar{p}u)_x + \left(\frac{2}{3}A\lambda T_x\right)_x + \eta\left[2u_x - \frac{2}{3A}(Au)_x\right]u_x - \frac{2}{3A}(Au)_x\bar{p} + \frac{2A}{3}\left(\frac{\delta U}{\delta t} + Q - L\right), \tag{3}$$

where the quantities are the atomic ion (e.g., O^+ and H^+) concentration $\bar{n}$, particle flux $\bar{n}u$, and partial pressure $\bar{p}$; overbars denote quantities multiplied by A, the cross-sectional area of the flux tube. The bulk velocity u is derived from the particle flux and the species temperature T can be obtained from $\bar{p} = \bar{n}\kappa T$, where κ is the Boltzmann constant. Subscript t refers to a partial derivative with respect to time and the subscript x refers to a partial derivative with respect to space along the magnetic flux tube. In Eq. (1) α and β denote the ion production rate and the loss frequency due to photochemical reactions and resonant charge exchange, respectively. In Eq. (2), E refers to the polarization electric field, which can be derived from the electron momentum equation, $g(\mathbf{r})$ is the gravity at point $\mathbf{r}$, and η is the viscous coefficient, which depends on the species density and temperature as well as the effective collision frequency defined by Schunk [2]. The quantities ν_k and Φ_k are the momentum

transfer collision frequency and the velocity-dependent correction factor, respectively. The summation over the index k is for all of the ion and neutral species except the one being simulated. In Eq. (3), λ represents the heat conductivity, which is normally proportional to the ion or electron temperature to the power of $5/2$. The term $\delta U/\delta t$ represents the rate of energy transfer due to elastic collisions between the different charge and neutral species. The quantities Q and L refer to the local electron heating and cooling rates, respectively.

The electron density can be determined from the quasi-neutrality condition $n_e = \sum_k n_k$ where subscript e indicates the electron species, $k = 1, 2, 3, 4, 5$ indicate H^+, O^+, N_2^+, O_2^+, and NO^+, respectively. Likewise, the electron bulk velocity can be determined by the ambipolar flow condition as $u_e = (1/n_e)\sum_k n_k u_k$. In Eq. (2), E represents the polarization electric field between ion and electron species, $E = -(1/eN_e)(\partial p_e/\partial x)$ which can be derived from the electron momentum equation by dropping all the inertial terms.

Equations (1) through (3) are Navier–Stokes equations. Equation (1) is the conservation law for the plasma species concentrations with allowance for sources. Equation (2) is a momentum conservation law, which includes a viscous term that is normally weaker than the convection term in the domain of smooth solutions. The plasma temperature can be found by solving Eq. (3) for the partial pressure, but the nonlinear heat conduction term has to be included, in addition to the convection term and the various heating and cooling processes.

If the equations are dominated by dissipative processes over convective transport, one can find methods other than FCT to solve them. Some implicit schemes work well in solving systems of the parabolic type. In ionospheric thermal plasma flows, viscosity is often weak, in comparison with other terms in the momentum conservation law, and one can attempt to neglect it and solve the momentum equation by the FCT technique alone. In contrast, the energy equations, particularly the electron equation, are dominated by heat conduction, which the FCT technique cannot handle well. Implicit algorithms work well for heat conduction, but they require solving a block-tridiagonalized matrix at each time step if one wants to solve the system simultaneously. Most implicit schemes work well when the domain of dependence is large [7, 8], but numerical smearing is inevitable when the flow becomes inviscid. Considering all of these issues, we looked for a method that works well for both nondissipative and strongly dissipative systems, and the coupled FCT–ADE method appears to be the most appropriate.

3. THE FLUX-CORRECTED TRANSPORT TECHNIQUE

Considering a convected quantity $u(x, t)$ with spatial variable x and temporal variable t, its simplest evolution is guided by a scalar conservation law of the form

$$u_t + f(u)_x = 0, \tag{4}$$

where $f(u)$ is the flux function of u.

The two-level explicit difference scheme applicable to Eq. (4) can be written as

$$U_j^{n+1} = U_j^n - \frac{k}{h}[F(U^n; j) - F(U^n; j-1)], \tag{5}$$

where U is normally the cell averaged value of u, h is the grid spacing, k is the time step, and F is the numerical flux function of two or more adjoining grid data U, which is a natural

result of the finite domain of dependence of the convection process. To avoid converging to a nonsolution, F is normally expressed in conservation form; theory and examples have been given by LeVeque [9] and references therein.

Due to the nonlinearity of Eq. (4), the convergence of Eq. (5) requires a consistent and conservative numerical method to be TV-stable; that is, the total variation of all the grid functions, U, defined over N discrete grids of the whole computational domain,

$$\mathrm{TV}(U) = \sup \sum_{j=1}^{N} |U_j - U_{j-1}|, \tag{6}$$

is at any time uniformly bounded by the total variation of the initial data. To guarantee that a numerical method has all of the above properties, the total variation diminishing (TVD) concept is broadly used as a quantitative description for algorithms designed for a nonlinear convection process. One importance of TVD is that a true solution to a scalar conservation law has this property; i.e., entropy solutions or vanishing viscosity solutions of Eq. (4) have nonincreasing total variations. Another feature of TVD is that any TVD method has the mathematical property of monotonicity preserving, which guarantees physical positivity in any convective transport process. This is very important for inviscid flow, where some second-order methods like Lax–Wendroff may fail in preserving monotonicity arising from numerical dispersion, particularly near discontinuities. Although these algorithms are of second-order accuracy for scalar conservation laws, they are of third-order accuracy for an appropriate dispersive equation, as was shown by the theory of modified equation [10]. Hence, oscillations are inevitable when using these algorithms. Once oscillations occur, total variations of the grid function also increase with time, and thus the algorithms are not TVD nor monotonicity preserving. As a result of numerical oscillations, a negative mass may occur, which violates physical positivity.

To evaluate the quality of an algorithm, another important criterion besides TVD concerns the spatial resolution, where at least second-order accuracy is needed on smooth solutions and discontinuities are accurately resolved. First-order approximations like the upwind method have been shown to satisfy the TVD and, hence, are monotonicity preserving, but they introduce numerical diffusion into the grid function, which may grow particularly large near a discontinuity so that nonlinear waves like shocks or contact discontinuities are severely smeared. Hence, they are not a high-resolution method.

To obtain a method that satisfies TVD and has a high resolution, one can use a high-order scheme for smooth solutions and a low-order scheme to increase the amount of numerical dissipation in the neighborhood of discontinuities to prevent numerical dispersion. A possible approach is to introduce some artificial viscosity into a known high-order numerical scheme, say, the Lax–Wendroff scheme, and then the numerical scheme will have the form

$$\begin{aligned} U_j^{n+1} = U_j^n - \frac{k}{h}\Bigg\{ & \frac{h}{2k}\varepsilon_{j+\frac{1}{2}}\left(U_{j+1}^n + U_j^n\right) + \left[\frac{h}{2k}\varepsilon_{j+\frac{1}{2}}^2 + hQ\right]\left(U_{j+1}^n - U_j^n\right) \\ & - \frac{h}{2k}\varepsilon_{j-\frac{1}{2}}\left(U_j^n + U_{j-1}^n\right) - \left[\frac{h}{2k}\varepsilon_{j-\frac{1}{2}}^2 + hQ\right]\left(U_j^n - U_{j-1}^n\right)\Bigg\}. \end{aligned} \tag{7}$$

In Eq. (7), $\varepsilon_{j+1/2} = k f_u(u)/h$ represents the courant number, which never exceeds 1 in any explicit algorithm due to the finite characteristic speed of $f_u(u)$. The last term represents the artificial viscosity added to the scheme, which will vanish when k approaches

zero. Although for constant Q Eq. (7) remains second-order accurate, it is not TVD nor monotonicity preserving, as was stated in Godunov's theorem; any linear, monotonicity preserving method should be at most first-order accurate. Therefore, the properties of TVD and high resolution seem to be mutually exclusive for linear methods. For the nonlinear artificial viscosity approach, however, it is not obvious how to determine the nonlinear viscosity coefficient $Q(U; j)$ so that it introduces just enough dissipation to satisfy TVD without causing unnecessary smearing.

To circumvent this dilemma, many nonlinear algorithms were invented. These algorithms are intuitive and usually there is a close connection between methods developed by quite different means. The two categories of flux-limiter and slope-limiter methods [9] are good examples of these and possess features of both TVD and high resolution. We present here the flux-limiter method developed by Boris *et al.* [12] in the following notes.

Any high-order numerical flux function, F_{H}, can be viewed as consisting of the low-order flux, F_{L}, plus a correction as

$$F_{\mathrm{H}}(U; j) = F_{\mathrm{L}}(U; j) + [F_{\mathrm{H}}(U; j) - F_{\mathrm{L}}(U; j)]. \tag{8}$$

In the flux-limiter method, a flux limiting process is applied to the flux difference in Eq. (8) so that it can be written as

$$F(U; j) = F_{\mathrm{L}}(U; j) + \Phi(U, \nabla U; j)[F_{\mathrm{H}}(U; j) - F_{\mathrm{L}}(U; j)], \tag{9}$$

where $\Phi(U, \nabla U; j)$ represents the flux-limiter, which functionally depends on the grid function U and its spatial gradient. If Φ approaches 1, Eq. (9) represents a high-order flux function applicable wherever U shows smooth distributions over some computational domain. On the other hand, if Φ approaches 0, then the flux function (9) degrades to a low-order numerical flux, which may be used in the vicinity of a discontinuity to maintain TVD. For Φ between 0 and 1 exclusively, Eq. (9) remains first-order accurate.

In the version of Boris and others [11], the low-order flux function can be expressed as a combination of the upwind flux and the Lax–Wendroff flux, where the upwind flux can be written as

$$F_{\mathrm{UW}}\big(U_j^n, U_{j+1}^n\big) = \frac{1}{2}\lambda_{j+1/2}\big(U_j^n + U_{j+1}^n\big) - \frac{1}{2}|\lambda_{j+1/2}|\big(U_{j+1}^n - U_j^n\big) \tag{10}$$

and where $\lambda_{j+1/2}$ represents the characteristic speed evaluated at the interface between grids j and $j+1$. Equation (10) is more diffusive than the Lax–Wendroff flux, which can be written as

$$F_{\mathrm{LW}}\big(U_j^n, U_{j+1}^n\big) = \frac{1}{2}\lambda_{j+1/2}\big(U_j^n + U_{j+1}^n\big) - \frac{k}{2h}\lambda_{j+1/2}^2\big(U_{j+1}^n - U_j^n\big). \tag{11}$$

The low-order flux-function chosen by Boris *et al.* [11] can be written as

$$F_{\mathrm{L}}\big(U_j^n, U_{j+1}^n\big) = \frac{1}{2}\lambda_{j+1/2}\big(U_j^n + U_{j+1}^n\big) - \gamma_{j+1/2}\big(U_{j+1}^n - U_j^n\big), \tag{12}$$

where $\gamma_{j+1/2}$ represents the numerical diffusion coefficient, which varies between $\frac{1}{2}|\lambda_{j+1/2}|$ and $\frac{k}{2h}\lambda_{j+1/2}^2$, so that Eq. (12) gives a first-order numerical flux that is less diffusive than (10)

and less dispersive than (11). The practical choice of the numerical diffusion coefficient $\gamma_{j+1/2}$ given by Boris and Book [12] was

$$\gamma_{j+1/2} = \frac{h}{k}\left(\frac{1}{6} + \frac{1}{3}\varepsilon_{j+1/2}^2\right). \tag{13}$$

This choice brings just a sufficient amount of numerical diffusion into the computational domain so as to prevent unphysical oscillations, to ensure physical positivity near a steep change of the grid function, and to maintain TVD. Nevertheless, the extra numerical diffusion resulting from this low-order numerical flux function can deteriorate solutions at domains of a smooth grid function. To remove extra numerical diffusion and keep second-order accuracy on a smooth domain, a flux-limiting or flux-correcting process is followed. Using the Lax–Wendroff flux function (11) as F_{H} and subtracting F_{L} given in (12) results in a numerical flux function of the form

$$F_{\mathrm{H}}(U; j) = F_{\mathrm{L}} + \mu_{j+1/2}\left(U_{j+1}^n - U_j^n\right), \tag{14}$$

where the term added to F_{L} represents the antidiffusion defined by Boris *et al.* [11], with the antidiffusive coefficient chosen as

$$\mu_{j+1/2} = \frac{h}{k}\left(\frac{1}{6} - \frac{1}{6}\varepsilon_{j+1/2}^2\right). \tag{15}$$

With use of (13) and (15), Eq. (14) reproduces the Lax–Wendroff numerical flux function. In other words, the antidiffusive coefficient (15) gives the maximum antidiffusion possible without violating TVD on a smooth domain. At a discontinuity, however, it requires a correction; otherwise the antidiffusive flux chosen above tends to create or accentuate local extrema. Thus, a flux-limiter, or flux-corrector, is introduced to replace the antidiffusive flux in (14), which prevents unphysical oscillations at the vicinity of a discontinuity. The flux-limiter given by Boris *et al.* [11] can be written as

$$f_{j+1/2}^{\mathrm{c}} \equiv S \cdot \max\left\{0, \min\left[S\frac{h}{k}\left(U_{j+2}^L - U_{j+1}^L\right), \left|\mu_{j+1/2}\left(U_{j+1}^L - U_j^L\right)\right|, S\frac{h}{k}\left(U_j^L - U_{j-1}^L\right)\right]\right\} \tag{16}$$

with $S = \mathrm{sign}\left(U_{j+1} - U_j\right)$, superscript L refers to intermediate values calculated with the low-order flux (12), which reduces the residual diffusion even further [11]. Equation (16) was designed to filter local maxima or minima and to prevent large antidiffusion when a sudden change in the grid function occurs between grids j and $j+1$.

To have a more intuitive and quantitative view of Eq. (16), we introduce here an absolute local variation function LV, as opposed to a total variation function, as

$$\mathrm{LV}\left(U; j + \frac{1}{2}\right) = \sum_{\mathrm{k}=-\mathrm{m}}^{\mathrm{m}} |U_{j+k+1} - U_{j+k}| \tag{17}$$

which samples a particular segment of the total variation between grid points $j - m$ to $j + m + 1$, with the length depending on the m value. The first quantitative sense of Eq. (17) is its capability of identifying local extrema when referred to a monotone data profile. It

is easy to see that any monotone change bounded by the two end data points, $j-m$ and $j+m+1$, has the same value of absolute local variation, above which are contributions of local extrema. Henceforth, any local maxima or minima can be identified by the difference between the absolute local variation defined in (17) and the absolute local variation of the two end data points $j-m$ and $j+m+1$. Thus, we have the following relative local variation concept, or simply the local variation,

$$\mathcal{LV}\left(U; j+\frac{1}{2}\right) = \sum_{k=-m}^{m} |U_{j+k+1} - U_{j+k}| - |U_{j+m+1} - U_{j-m}| \tag{18}$$

which describes the relative deviation of the grid function from a monotone change bounded by the two end data points. Obviously, any local maxima or minima can lead to the value of $\mathcal{LV}$ greater than 0, while a monotone change always make $\mathcal{LV}$ vanishing. The local variation function we have introduced is defined at the interface between cells j and $j+1$. By choosing four neighboring grid points around the interface, we can identify all the extrema as Eq. (16) does. As long as $\mathcal{LV}$ is greater than 0, we add in all the antidiffusion, which acts to eliminate local extrema the same way that Eq. (16) does, and hence, a TVD scheme is maintained.

Local variation can single out local extrema, but cannot distinguish shocks or contact discontinuities from smooth variations because both are monotone and $\mathcal{LV}$ vanishes. The identification of a shock or contact discontinuity from other monotone profiles is usually done by comparing the spatial gradients at adjoining data pairs. If a gradient at the interface is much larger than values at the two neighboring interfaces, the antidiffusion is held at the smallest value of the gradient to maintain a certain amount of numerical diffusion in the flux function to prevent oscillations. Denoted by ∇, the difference between two neighboring points, or the absolute local variation of the adjoining data pair, Eq. (16) can be expressed as

$$F^c_{j+1/2}(U; j) = 0 \quad \text{if } \mathcal{LV} > 0 \tag{19}$$

$$F^c_{j+1/2} \equiv \min\left[\left|\nabla U^L_{j+3/2}\right| h/k, \left|\nabla U^L_{j+1/2}\right| \mu_{j+1/2}, \left|\nabla U^L_{j-1/2}\right| h/k\right] \quad \text{if } \mathcal{LV} = 0. \tag{20}$$

The final numerical flux, including the limiter in Boris's version, can be written as

$$F(U^n; j) = F_{\mathrm{L}}(U^n; j) + F^c_{j+1/2}. \tag{21}$$

For $\mathcal{LV} > 0$, Eq. (21) represents a low-order flux-function (upwind) given by (12); for $\mathcal{LV} = 0$, Eq. (21) represents a high-order flux-function (Lax–Wendroff) given by (11). The FCT version given by Boris is implemented by substituting (21) into (5). Its TVD and high resolution qualities are established through the above analysis.

Although limiter (19) filters local extrema, it also eliminates real physical extrema. In addition, determining a discontinuity by Eq. (20) relies subjectively on intuition. As a matter of fact, the clipping effect at physical extrema and the errosive effect at neighbors of a discontinuity become new problems, as shown by passive convection tests in [11]. Although the flux-limiter was improved by Zalesak [13] and Kunhardt *et al.* [14], particularly in preserving local physical extrema, there are still hard problems to be solved. When applied to ionospheric thermal plasma flows, however, the inaccuracy caused by a flux-limiter is not important due to the existence of physical dissipation. The above notes were presented

to help explain the flux-corrected transport technique developed by Boris, so that it can be used appropiately. Although the proposed local variation may be useful in exploring a more precise flux-limiter, a further investigation of inviscid algorithms is not in the current research.

4. THE FCT–ADE METHODS

As mentioned above, the flux-corrected transport technique can be applied to solve the nonlinear convection process efficiently. However, a problem arises when we apply this technique to solve the Navier–Stokes system of Eqs. (1), (2), and (3) with dissipation terms included. Unlike convection, mathematically, viscosity and heat conduction are represented by second-order spatial derivative terms; computationally, they have an infinite domain of dependence; and physically, they transport momentum and energy through thermal motion guided by statistical mechanics. Although particle diffusion is not explicitly shown in Eqs. (1), (2), and (3), it can be evaluated when the convective velocity is sufficiently small. All dissipative processes have a similar mathematical formulation. If we separate these processes from convection and local chemical reactions, then a typical dissipation process can be written as

$$u_t = [\alpha(u)u_x]_x, \tag{22}$$

where the dissipative coefficient, $\alpha(u)$, is normally a function of the dependent variable u. In contrast to the numerical dissipation brought about by a low-order convection scheme, the physical dissipation does not vanish as the grid is successively refined.

To solve Eq. (22), an explicit scheme, forward in time and centered in space (FTCS), was adopted and incorporated with the FCT technique to model the two-dimensional flame process by Patnaik *et al.* [15]. The detailed model subcycles the viscosity and heat conduction processes within the time step set up for stability of the nonlinear convection processes. The advantages of this explicit scheme are the ease of programming and computational time saving, compared with an implicit scheme. Defects of this technique are its first-order truncation error and stability limitations. An implicit scheme yields second-order accuracy and unconditional stability; however, a tridiagonal matrix has to be solved within each time step. Again, this is not desired in attempting to solve for the species densities, velocities, and temperatures simultaneously in our detailed modeling.

Among all the numerical schemes designed for physical dissipative processes, the alternating-direction explicit (ADE) scheme, developed by Barakat and Clark [6], has all of the desired properties of a second-order local truncation error and unconditional stability. To illustrate this simple and efficient scheme, we first look at the case when the dissipative coefficient, α, is a constant. Let V_i and W_i be the solutions of the following two-step finite difference representations of Eq. (22). Then, the ADE scheme can be written as the following two-step operation:

$$V_j^{n+1} = V_j^n + \frac{k}{h}\left[\frac{\alpha}{h}\left(V_{j+1}^n - V_j^n\right) - \frac{\alpha}{h}\left(V_j^{n+1} - V_{j-1}^{n+1}\right)\right] \tag{23}$$

$$W_j^{n+1} = W_j^n + \frac{k}{h}\left[\frac{\alpha}{h}\left(W_{j+1}^{n+1} - W_j^{n+1}\right) - \frac{\alpha}{h}\left(W_j^n - W_{j-1}^n\right)\right]. \tag{24}$$

The final solution of Eq. (22) is simply the arithmetic average of Eqs. (23) and (24)

$$U_j^{n+1} = \left(V_j^{n+1} + W_j^{n+1}\right)/2. \tag{25}$$

In the application of this method, Eq. (23) marches the solution from the left boundary to the right boundary. While marching in this direction, V_{j-1}^{n+1} is already known, consequently, V_j^{n+1} can be determined explicitly. Likewise, Eq. (24) marches the solution from the right boundary to the left boundary, resulting in an explicit solution since W_{j+1}^{n+1} is already known. Since Eqs. (23) and (24) are not coupled, both can be solved simultaneously, resulting in an efficient explicit scheme. Furthermore, in comparison with some first-order explicit schemes and some second-order implicit schemes, discrete values of U_j^{n+1} had been tested numerically to yield the lowest local truncation error [6].

To apply this numerical scheme to our ionospheric thermal plasma flow model, we need to rewrite Eqs. (23) and (24) in conservation form and on a variably spaced grid. The conservation form of these equations can be written as

$$V_j^{n+1} = V_j^n + \frac{k}{h}\left[\frac{\alpha_{j+1/2}^n A_{j+1/2}}{\Lambda_j}\left(V_{j+1}^n - V_j^n\right) - \frac{\alpha_{j-1/2}^{n+1} A_{j-1/2}}{\Lambda_j}\left(V_j^{n+1} - V_{j-1}^{n+1}\right)\right] \tag{26}$$

$$W_j^{n+1} = W_j^n + \frac{k}{h}\left[\frac{\alpha_{j+1/2}^{n+1} A_{j+1/2}}{\Lambda_j}\left(W_{j+1}^{n+1} - W_j^{n+1}\right) - \frac{\alpha_{j-1/2}^n A_{j-1/2}}{\Lambda_j}\left(W_j^n - W_{j-1}^n\right)\right], \tag{27}$$

where Λ_j denotes the cell volume labeled j, and $A_{j+1/2}$ denotes the interface area between grid points j and $j+1$. The superscript on α indicates a time dependence of the dissipative coefficient. For the ionospheric thermal structure, α is not only a function of the species densities, but also an exponentially increasing function of the species' temperature too. The thermal conductivities of the atomic ion and electron species are scaled as $T^{5/2}$, resulting in strong nonlinear heat conductions. Strictly speaking, a precise solution calls for many iterations on Eqs. (26) and (27) within each time step. Because this is time-consuming, it is not applicable for our detailed modeling of ionospheric thermal plasma flow.

A usual way to deal with nonlinear dissipation is to expand the thermal conduction coefficient α in time, so that it can be truncated at any degree of approximation. In our detailed modeling, α is simply linearized in time by replacing values at time level $n+1$ with values at level n. The inaccuracy brought about by this method is of the same order of magnitude that arises from time splitting. However, because the rate of change of the species temperatures has a much larger time scale compared to the time step set for TV-stability of the corresponding convective processes, our numerical tests have shown that these inaccuracies do not grow using the time step set for convection.

Because the nonlinear dissipative coefficients given by Eqs. (26) and (27) are interface values and because our viscous coefficients and heat conductivities are evaluated on grids with a variable spacing along a magnetic flux tube, we need to find the interface values by interpolation. To find the dissipative coefficients at the interface locations, the flux-matching method given by Oran and Boris [16] has been used. The basic idea behind this method is that the flux evaluated from the left-hand side of the interface should match the one from the right-hand side; thus a flux-weighted dissipation coefficient, $\alpha_{j+1/2}$ can be

determined as

$$\alpha_{j+1/2} = \frac{\alpha_j \alpha_{j+1}(x_{j+1} - x_j)}{\alpha_{j+1}(x_{j+1/2} - x_j) + \alpha_j(x_{j+1} - x_{j+1/2})}, \tag{28}$$

where x_j represents the arc-length of the magnetic flux tube at grid j measured from the lower boundary of the northern ionosphere. Equation (28) ensures the fewest inconsistencies in the fluxes at all interfaces while solving Eqs. (26) and (27).

So far, we have introduced the flux-corrected transport technique to handle the nonlinear convection process and the alternating-direction explicit method for dissipative processes. We also need to find a way to handle chemical reactions. In numerical simulations of reactive flows, the time evolution of a conserved quantity resulting from chemical reactions is normally treated as solutions of the ordinary differential equations of chemical kinetics. Many possible interactions among different physical and chemical processes, as well as ways of decoupling and solving chemically reacting processes, can be found in Oran and Boris's book [16]. Chemical reactions, particularly for inviscid flows with stiff sources, yield more difficulties, regardless of the ways of coupling. In solving a scalar conservation law with stiff chemical reacting sources, LeVeque and Yee [17] used a time-splitting method and a predictor–corrector method of the MacCormack type and numerically compared the solutions for the same reacting scalar conservation law. It was found that, although both methods were second-order accurate in space and time, they gave incorrect propagation speeds for discontinuities convected by an inviscid flow with stiff reacting sources. Under normal situations, both methods can track discontinuities precisely as long as the reacting sources are not too stiff. Since our model includes viscosity and heat conduction processes, which always tend to smear shocks arising from nonlinear convection, the concern about an accurate speed of shock propagation becomes irrelevant.

As was shown by Boris *et al.* [11], reacting sources and nonlinear convection processes can be coupled through a time-splitting technique. Second-order accuracy can be achieved by using a two-stage Runge-Kutta time integration for reacting sources. In the first stage, provisional values are predicted through a forward-in-time integration for a half time step. Then, based on these provisional values, a centered-in-time-and-space integration is implemented in the second stage to find the results at the end of the whole time step. More details can be found in [11].

Figure 1 shows the flowchart for the time marching process for a whole time step. At the beginning, initial values are used to evaluate sources, upon which state variables are forwarded in time by half a time step. Using these state variables as provisional values, a convective transport process is implemented using the FCT technique, which advances variables by half a time step (i.e., the level $n + 1/2$). Based on these intermediate variables, subsequent time-centered integrations on sources, convection, and dissipation are implemented successively, and thus variables are advanced in time by a whole step.

As a result of numerical tests, it turns out that, even though we do not evaluate viscosity and heat conduction at the half time-step level, the variables do not change appreciably. Because of that, we evaluate the dissipative processes only once within each whole time step. This saves computer time and works well as long as the time step is appropriately chosen so that strong heat fluxes imposed at the top boundary of the electron stream give convergent temperature profiles; illustrations will be given in the next section.

To see a typical splitting procedure implemented in the coupled numerical scheme, we pay particular attention to the numerical solution of Eq. (3), which includes all the processes

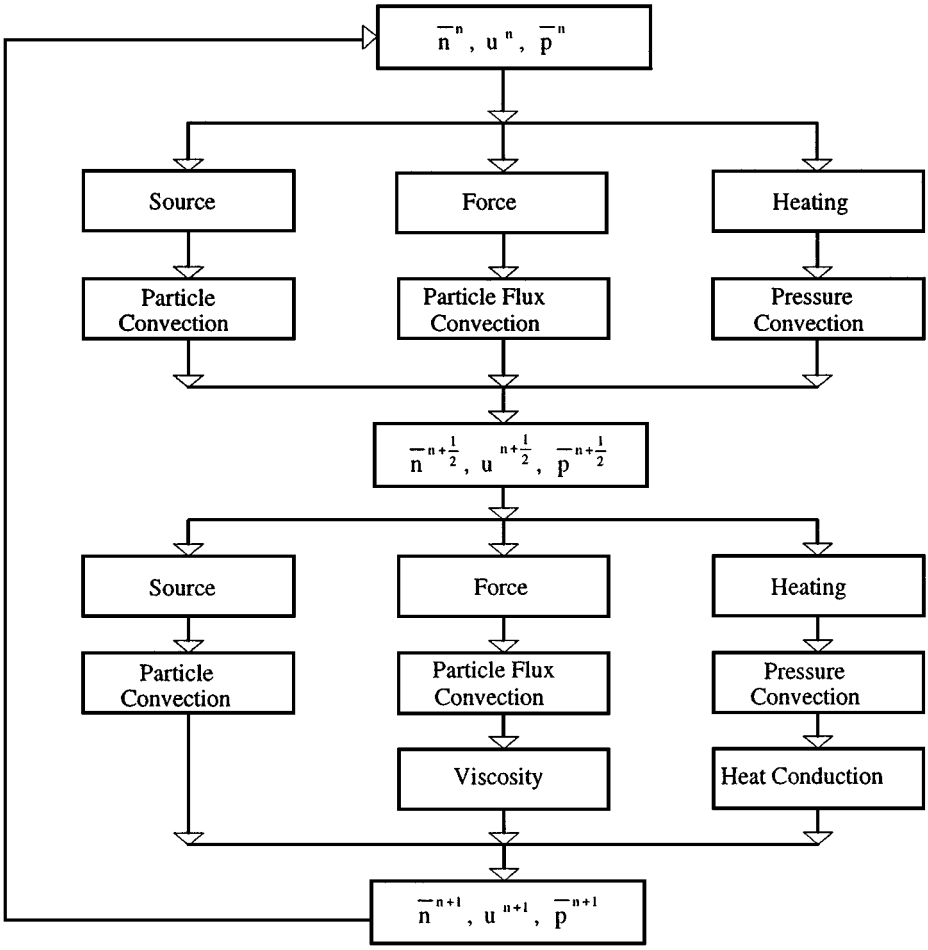

FIG. 1. Flowchart of the FCT–ADE time marching scheme. The superscripts n, $n + 1/2$, and $n + 1$ indicate values at the beginning, the half time step, and the whole time step, respectively.

we are concerned with. This equation accounts for the rate of change of partial pressure as a result of contributions from the different terms on the right-hand side. The first term represents the contribution from convection, the second term is the thermal conduction, the third term is customarily called the dissipation function, which represents the equivalent heating rate arising from mechanical energy release due to viscous deformation, the fourth term indicates the contribution from compression, and the last term includes all local heating and cooling processes external to the system being concerned. The mathematical structure of Eq. (3) can be concisely written as

$$u_t = -f(u)_x + [\alpha(u)u_x]_x + \Psi(u). \tag{29}$$

On the right-hand side of Eq. (29), the first term represents convection, the second term represents conduction, and the third term represents the sum of all the other terms on the right-hand side of Eq. (3) relating to the local heating and cooling processes. Let $\mathcal{H}$ be the operator standing for an explicit two-level numerical stencil, then the time-splitting

procedure given in Fig. 1 can be expressed as the following two stages:

$$U^{n+1/2} = \mathcal{H}_f^{k/2}(U^n)\mathcal{H}_\psi^{k/2}(U^n)U^n \tag{30}$$

$$U^{n+1} = \mathcal{H}_d^{k}(U^{n+1/2})\mathcal{H}_f^{k}(U^{n+1/2})\mathcal{H}_\psi^{k}(U^{n+1/2})U^n, \tag{31}$$

where the subscripts ψ, f, and d represent local heating, convection, and dissipation, respectively. Superscript k represents the time step length and the dependence of $\mathcal{H}$ on the argument U displays the nonlinear properties of these operators.

5. STEADY-STATE SOLUTIONS THROUGH THE TIME-DEPENDENT APPROACH

The ionospheric plasma is mainly composed of molecular (N_2^+, O_2^+, and NO^+) and atomic (O^+ and H^+) ions and electrons. Thermal plasma flows, however, are dominated by atomic ions and electrons, which maintain quasineutrality. Each species (O^+, H^+, and e^-) satisfies the Navier–Stokes system given by Eqs. (1), (2), and (3). Under certain initial distributions and appropriate boundary conditions, the Navier–Stokes systems can be solved by the proposed FCT–ADE method. Solutions march forward in time from the initial distributions giving both steady and time-dependent results for all the basic physical observables. Since our thermal plasma flow model is coupled both to an empirical neutral atmospheric model and to the nontransportive molecular ion photochemistry model, the steady-state solutions are obtained via a time-dependent simulation with constant inputs.

Before running each case, the computational domain is established along the selected magnetic flux tube, which starts at 42.6°N, 288.5°E at an altitude of 150 km, where the lower boundary of the computational domain is located. The choice of flux tube location is determined by the physics to be studied. At altitudes below 200 km, photochemical equilibrium is dominant and convection across the lower boundary can be neglected. By choosing the top boundary at 3000 km (33.8°N, 290.6°E) along the selected magnetic flux tube, where transport processes are dominant, unique solutions can be found by specifying density gradients, particle fluxes, and heat fluxes at that height. Since the Millstone Hill incoherent scatter radar site is located below the lower boundary of the chosen flux tube, that facilitates model-data comparisons and provides a way to judge the validity of our modeling results. Based on the characteristic scale lengths of the parameters, a one-dimensional computational domain is formed with a grid spacing that varies with altitude. The grid intervals, however, are restricted to be much less than the characteristic scale lengths of the parameters. Also, the increments between adjoining grid pairs are less than 1% of the grid spacing.

Owing to the complexities of the Navier–Stokes systems and the unknown initial conditions, a steady-state solution is usually obtained first before exploring any time-dependent behavior. The solutions, however, depend largely on the top boundary conditions, which have to be well posed and physically consistent. In our simulations, due to the vast number of protons uniformly stored in the plasmasphere, the H^+ density gradient is negligibly small at the upper boundary. For O^+, since the ionosphere is the only source of O^+ at high altitudes, an extrapolation through inner grids works well for values at the top boundary interface. The H^+ particle flux at the top is chosen as an input parameter that is adjusted to the interhemispheric flow conditions, supplying protons to the plasmasphere in the daytime and receiving protons from the plasmaphere at night. As a minor ion, the O^+ flux at 3000 km is simply neglected and the boundary interface is treated as a rigid wall. This allows us to estimate the

amount of O^+ that resides in the upper part of the flux tube in the daytime and subsequently flows down to the ionospheric F region at night. The electron density, determined by the quasineutrality condition, is a summation over all the molecular and atomic ion densities. The electron flux is determined by the no-current-flow condition. The electron stream has two major heat sources. One is the solar extreme-ultraviolet (EUV) heating and the other is the heat conducted down the flux tube from regions above the top boundary. This conducted heat flux is an adjustable input parameter to the electron energy equation. The heat fluxes of H^+ and O^+ across the top boundary are usually small and have been neglected. The densities of the molecular ions are determined by local photochemical reactions, and a thermal equilibrium is also assumed among all the molecular ion and neutral components. These photochemical and thermal equilibrium processes are evaluated by iteration at a different time step, usually much larger than the time step set by the CFL conditions.

Figures 2a, b, and c illustrate typical steady-state solutions of the species densities, velocities, and temperatures. To approach these solutions, a constant downward H^+ particle flux

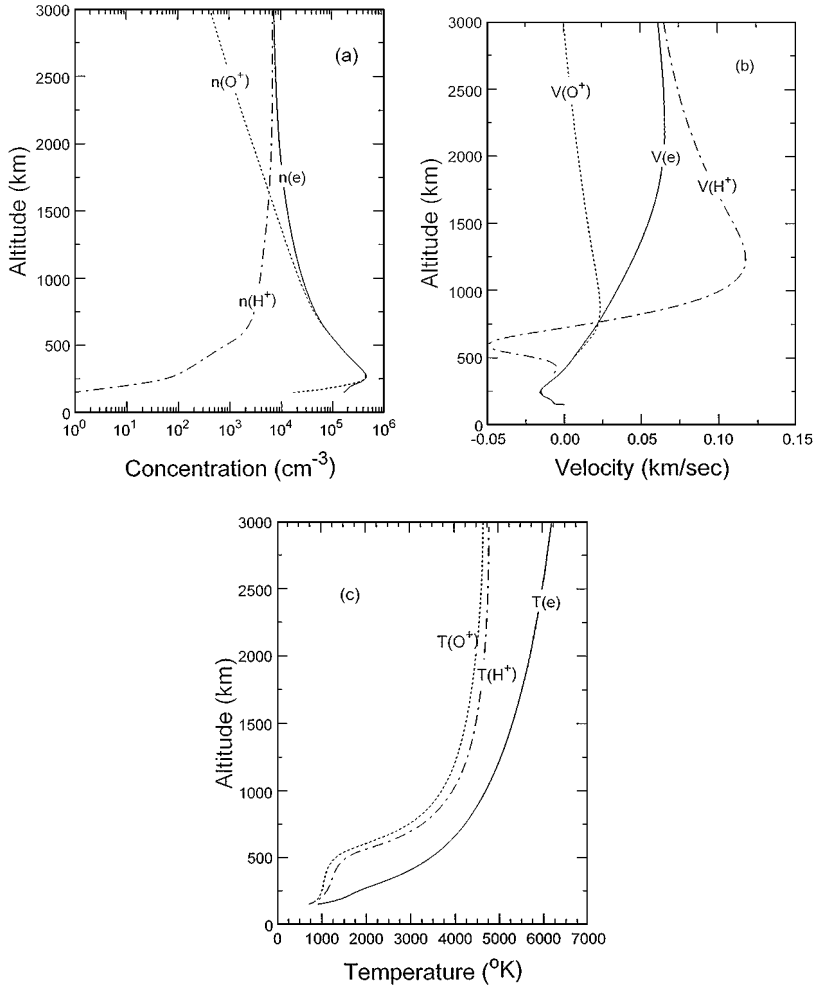

FIG. 2. Noontime steady-state solutions of (a) species densities, (b) species velocities, and (c) species temperatures.

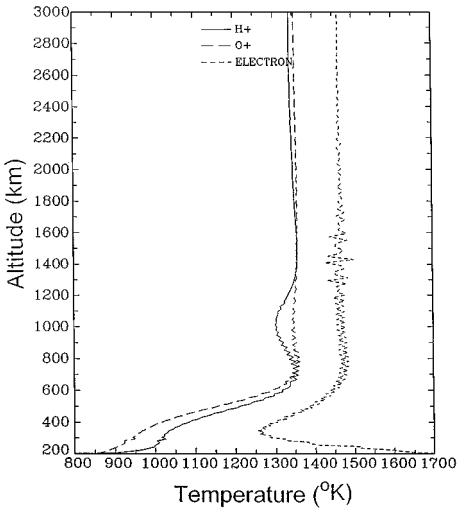

FIG. 3. Steady-state solutions of H^+ (solid line), O^+ (dashed line), and electron (dotted line) temperature profiles using the FCT–FTCS method. No electron heat flux was imposed at the top boundary.

(4.5×10^7 cm^{-2} s^{-1}) and a constant downward electron heat flux (-1.0×10^{10} eV cm^{-2} s^{-1}) where imposed at the top boundary; these are typical values. Note that the assumed initial conditions do not affect the final steady-state solution. As shown by the velocity profiles, the final steady plasma flows are basically subsonic, giving flow fields of a saturated flux tube with constant H^+ flux accross the top boundary, which is what is expected for a standard mid-latitude flow pattern at 1200 local solar time (LST).

In our attempt to solve the Navier–Stokes systems, we first used the FCT technique to solve the convection part and the FTCS scheme to solve the heat conduction part, and the final results were found at the end of each time step through a time-splitting technique. To avoid a stiff heat input, we simply omitted the heat flux that was previously imposed on the electron gas at the "top boundary," so that the local solar EUV heating at the low altitudes (below 400 km) was the only heat source external to the systems. In this scenario, energy transfer through conduction was comparable to convection at most altitudes. Shown in Fig. 3 is the steady-state solution for the species temperatures versus height obtained by using the FCT-FTCS method. Numerical oscillations are clearly seen in the plot. These temperature oscillations are caused by the FTCS scheme because its stability requires a much smaller time step than the one determined by convection. The large heat conductivity of the electron gas acts to reduce the time step considerably when this explicit scheme is used. Also, its accuracy is restricted to be first-order in time. The reason why these oscillations do not grow nonlinearly is that at each time step, soon after the oscillations are excited, the TVD properties of the FCT scheme act to smooth the numerical oscillations. On the other hand, the nonlinearly self-controlled antidiffusion tries to maintain these oscillations, which have a relatively large wavelength. The numerical oscillations do not grow infinitely large because we only consider a weak heat source. As a numerical test result, we found that any heat flux imposed on the electron gas at the top boundary would cause a numerical instability when the FCT-FTCS method was used.

In contrast, Fig. 4 shows the results of using the FCT–ADE method. Numerical oscillations are not present, even though the time step is the same. By comparing the two plots, the

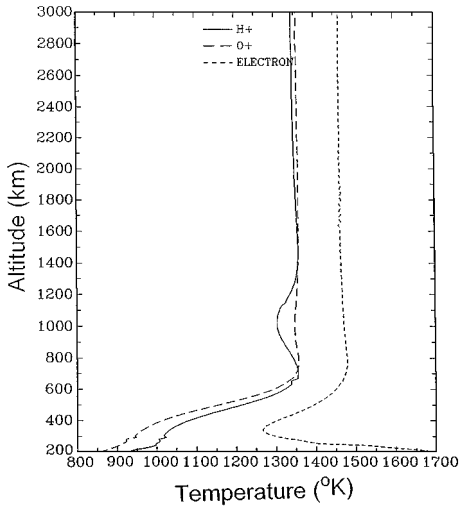

FIG. 4. Steady-state solutions of H^+ (solid line), O^+ (dashed line), and electron (dotted line) temperature profiles using the FCT–ADE method. No electron heat flux was imposed at the top boundary.

species temperature profiles are almost the same, except for the oscillations in Fig. 3. A comparison of the two methods suggests that the FTCS is applicable only through many subcycling processes within the time step set for the TV-stability of the corresponding nondissipative systems. Hence, it seems that an unacceptable subcycling is needed when a heat flux is imposed on the electron gas at the top boundary. However, all the problems encountered by the FCT-FTCS method are removed by the FCT–ADE method, which can cope with a strong heat conduction without a reduction in the time step.

Viscosity plays an important role in solving the coupled systems even though it is usually weak and often negligible in ionospheric modeling. To see effects of viscosity, we considered three different cases, obtained by multiplying the viscous coefficient by 0, 1, and 2, respectively. Figures 5a, b, and c show comparisons between inviscid flow (viscous coefficient multiplied by 0) and viscous flow (viscous coefficient multiplied by 1), where the thick lines represent viscous flow and the thin lines represent the inviscid flow, which is also indicated by a prime on each physical quantity. The densities in Fig. 5a show that the H^+ density is not sensitive to the viscous effect, but the O^+ density scale height is significantly elevated due to viscosity. The velocities in Fig. 5b indicate that the oscillations in the inviscid H^+ flow field are completely removed and the downward H^+ flow is significantly enhanced. Also, the upward O^+ flow is increased by the inclusion of viscosity. Although the electron temperature structure does not change much due to viscosity, as shown in Fig. 5c, the O^+ temperature can differ by about 100 K due to the direct result of viscous heating. The H^+ temperature profiles show less difference than the O^+ profiles but a larger difference than the electron profiles, which are not shown in the plot in order to present a clear view of the comparison.

Figures 6a, b, and c show the comparisons of the viscous flows calculated with the viscous coefficient multiplied by 1 and 2, respectively. Apparently, although the viscous coefficient is amplified by a factor of 2, the height profiles of density, velocity, and temperature remain unchanged. As a result of numerical testing, we conclude that viscosity has an effect on the minor ion species, but it has a negligible effect on the major ions and electrons.

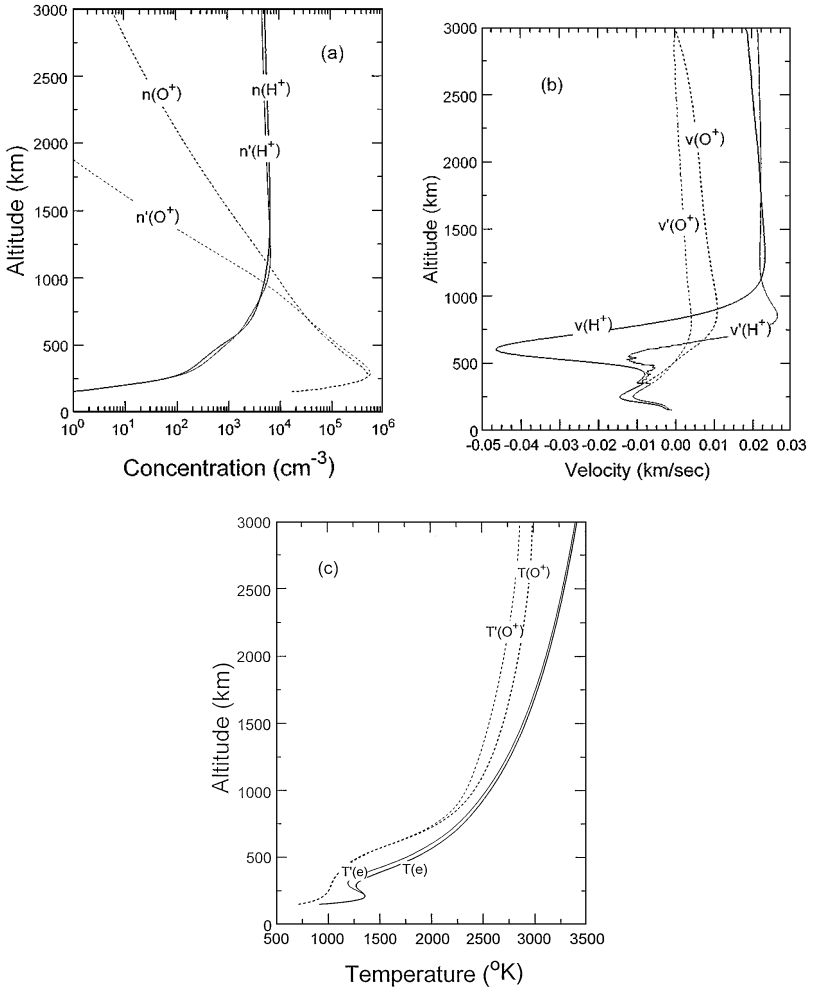

FIG. 5. Comparisons of inviscid flows (thin lines labeled with primed quantities) and viscous flows (thick lines) with coefficient multiplied by 1. Density, velocity, and temperature comparisons are shown in (a), (b), and (c), respectively.

In addition to viscosity, another important process for ionospheric thermal plasma flows is heat conduction, particularly for thermal electrons for which a downward heat flux is normally imposed at the top boundary. For a typical electron heat flux input, the implemented algorithm results in height profiles of plasma density, velocity, and temperature that converge in time. In particular, starting from the same initial profiles and the same heat flux input, the results are the same at any instance and converge to the same steady-state height profiles with the same speed, regardless of the time step used in the calculation. Convergence tests can fail, however, once the electron heat flux input exceeds a threshold of about 10^{11} eV/cm^2/s. Failure in the convergence reveals a numerical stiffness of the problem. In physics, such a strong heat flux may correspond to an ill-posed problem, since it is rarely seen in the mid-latitude ionosphere. Further discussions related to space physics will be presented elsewhere.

Further numerical tests have demonstrated that by removing the viscosity and imposing a strong electron heat flux at the top boundary, the H^+ velocity and the electron temperature

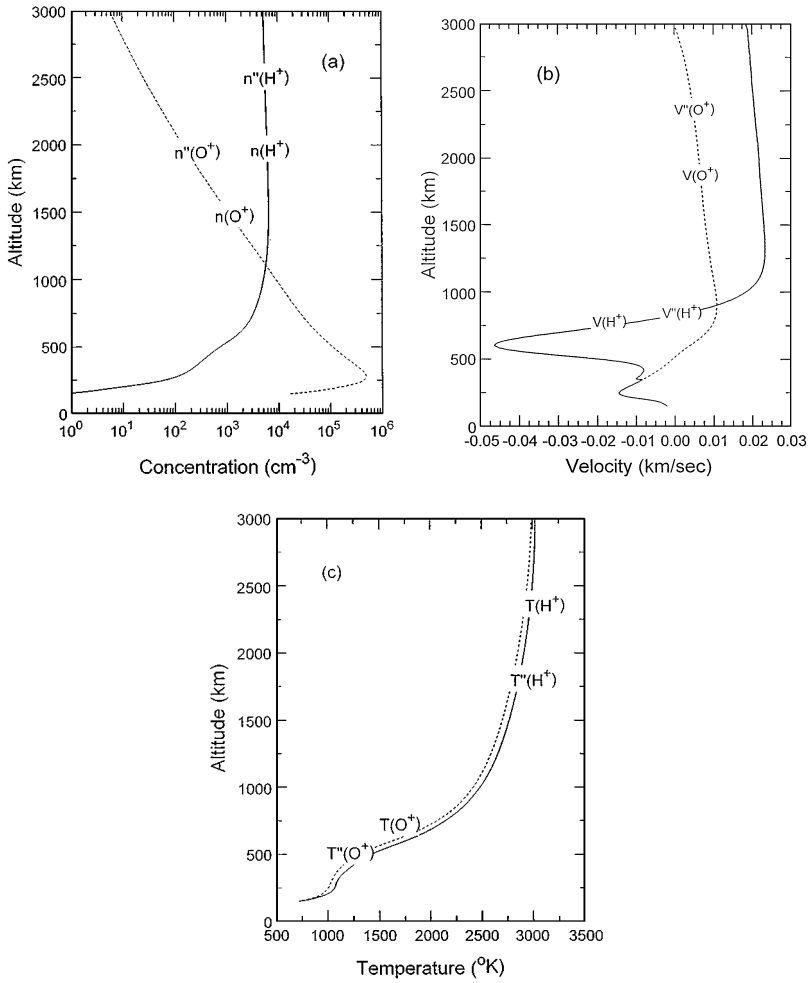

FIG. 6. Comparisons of viscous effects multiplied by 1 (thick lines) and 2 (thin lines labeled with double primed quantities), respectively. The panels correspond to: (a) density comparison; (b) velocity comparison; and (c) temperature comparison.

above about 1500 km show oscillations or wave propagation toward the top boundary, although the species' density profiles have no perceivable change. The wave behavior can become much more obvious if we allow O^+ to flow freely out of its top boundary. The periodic shock propagation seen in the O^+ gas may cause periodic oscillations of the electron density, which, is turn, may result in oscillations of the electron temperature. These waves are a result of the inviscid flow assumption, and they can be effectively removed by considering viscosity. Nevertheless, periodic waves in the inviscid flow occur only when the electron heat flux input approaches its threshold; again, that is rarely seen in the mid-latitude ionosphere.

6. TIME-DEPENDENT SOLUTIONS

Except around local noon, ionospheric plasma flows are mostly unsteady, particularly at sunrise and sunset when geophysical conditions change drastically in time. Therefore, a detailed modeling of the physics calls for a time-dependent simulation.

Exploring the time-dependent solutions for a particular day normally begins with some initial steady-state solutions, and then it proceeds in time until solutions are repeatable in a diurnal sense. Furthermore, one way to validate the time-dependent model results obtained with the FCT–ADE method is to compare with results from another model that is based on different algorithms. Since the USU time-dependent ionospheric model (TDIM) provides height distributions of plasma densities and temperatures, mainly O^+, O_2^+, N_2^+, NO^+, and electrons, it is convenient to compare our results with this model. Since numerical model results rely on the basic assumptions made in developing the model, it is worthwhile to have a clear view of major differences between our model and the USU–TDIM model: (1) The TDIM model was designed for the ionospheric *E* and *F* regions, which range from 100 km to 800 km, where O^+ is treated as the major atomic ion participating in transport. In contrast, the FCT–ADE model is valid for the above and, as previously mentioned, the computational domain is from 150 km to 3000 km. Here, both O^+ and H^+ are considered as major atomic ion species participating in transport. (2) In the TDIM, a diffusion formulation is used for the ion transport process, which limits the formulation to subsonic flows. With the FCT–ADE model, the complete continuity and momentum equations are solved, including the inertia terms. (3) The TDIM solves the systems along a dipolar magnetic flux tube using the implicit Crank–Nicolson scheme, while the FCT–ADE model solves the systems along the real magnetic flux tube using an explicit nonlinear algorithm. Despite the above differences, the TDIM is a valid model for the ionospheric *F* region, since photochemical reactions and O^+ diffusion are the major processes in this region. Also, the TDIM is a much faster model than the current model, owing to the above assumptions. Model comparisons are implemented between 150 km and 800 km, where the O^+ reactive and diffusive processes are dominant.

For the same geophysical inputs, comparisons of corresponding electron density and temperature profiles are illustrated in Figs. 7 and 8, respectively. In these plots, solid lines represent FCT–ADE model results, while dashed lines represent the USU–TDIM model results. It is obvious that the corresponding density and temperature profiles have very similar shapes, particularly at night, where the profiles tend to overlap. The largest difference is found at sunrise, when the external inputs change drastically in time. During the daytime, differences exist but they do not grow with time and diminish after sunset. These daytime differences are partly caused by the fact that different space and time steps were used in the two models and partly because of model differences. In particular, the FCT–ADE model includes H^+ and slightly different electron energy transfer processes. At any rate, the differences between the two models are not important physically because the input parameters needed by the ionospheric models (neutral densities, temperatures, winds; collision cross sections; chemical reaction rates; etc.) have a large uncertainty and the two models agree within this uncertainty.

Further differences in the density profiles are also noticed below about 200 km. They are partly caused by the routines solving for the molecular ion transport. In the TDIM model, the molecular ion species are both reactive and diffusive, while in the FCT–ADE model, the diffusive effect is neglected and photochemical equilibrium for molecular ions is assumed. However, the difference in the molecular ion densities calculated by the flow models is also partly due to the difference in the calculated electron temperatures at low altitudes. The electron temperature affects the molecular ion recombination rates, which then affect the molecular ion densities. Again, this difference between the two models is not important physically because of the uncertainties associated with the input parameters.

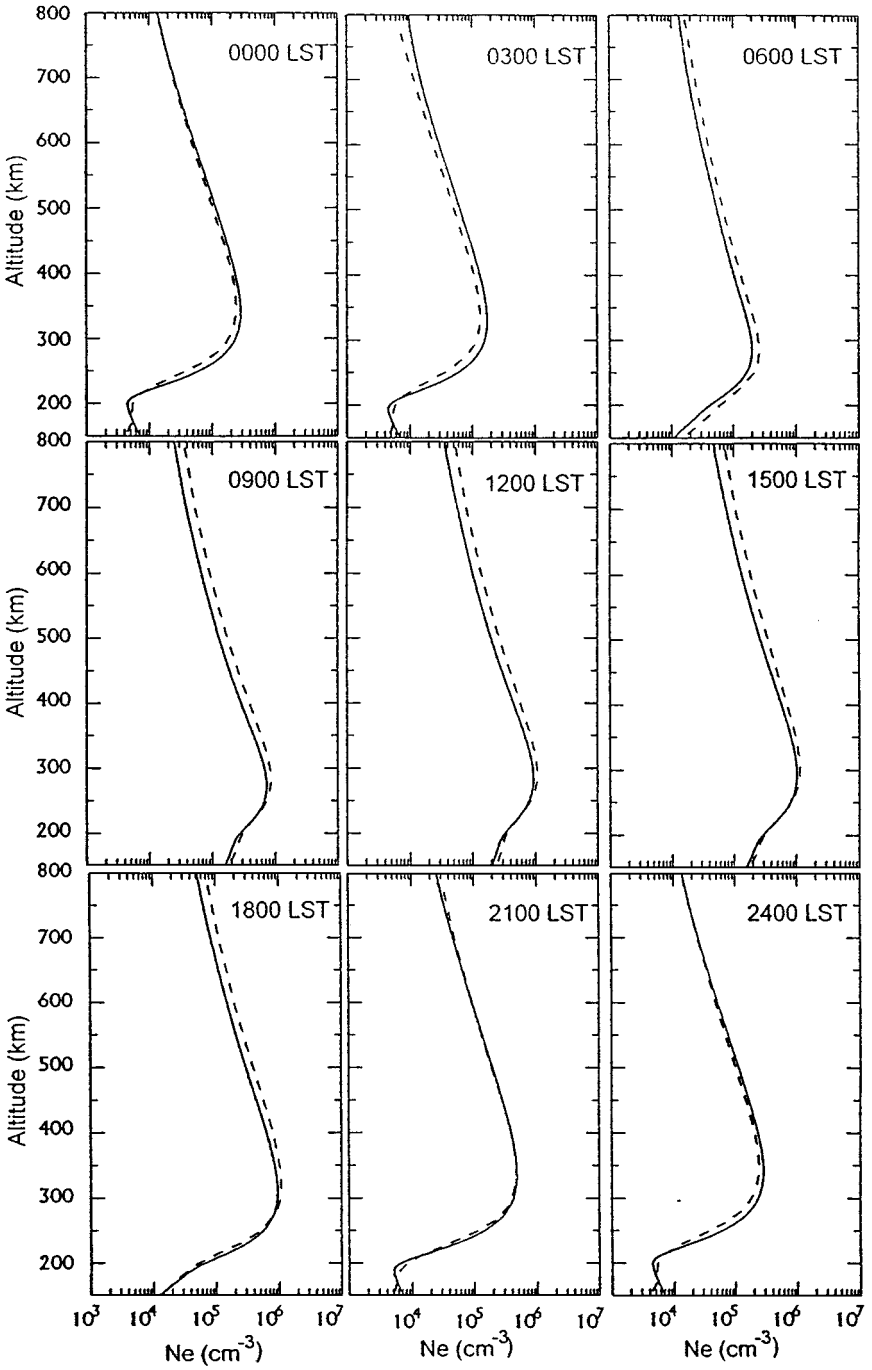

FIG. 7. Comparison of time-dependent electron density profiles. Solid lines represent FCT–ADE model results and dashed lines represent USU–TDIM model results.

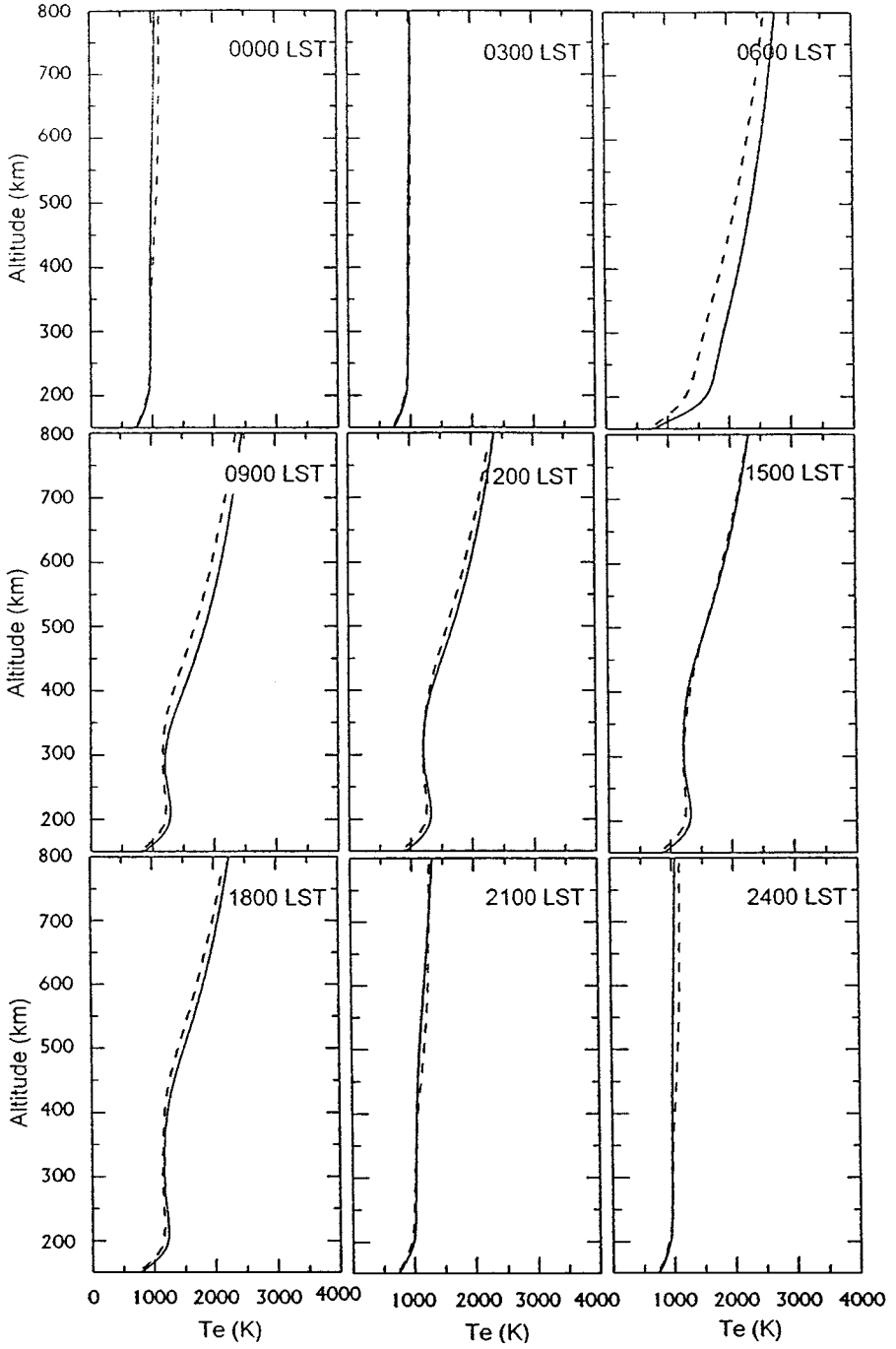

FIG. 8. Comparison of time-dependent electron temperature profiles. Solid lines represent detailed FCT–ADE model results and dashed lines represent USU–TDIM model results.

Besides a comparison with another model, our results have also been compared with the ionospheric incoherent scatter radar data given by Wickwar *et al.* [18]. As an important application of the FCT–ADE model, the so-called anomalous *F* region density maximum has been explained. This is another illustration of the model validity. Further details can be found in the referred paper, which is in preparation.

7. CONCLUSIONS

We have introduced the local variation concept to understand the flux-limiter in the flux-corrected transport technique. We have also coupled this technique with the alternating-direction explicit method in a time-splitting fashion to solve the multiple systems of Navier–Stokes equations with weak viscosity and strong heat conduction. Numerical tests have been conducted for both steady-state and time-dependent situations. Viscous effects and heat transfer were examined through convergence tests, while the time dependence of state variables was studied through a model comparison. The fully coupled FCT–ADE numerical techniques give simultaneous solutions of the complicated systems, and the results are consistent with solutions obtained from a completely different method. The combined FCT and ADE methods give a new approach to chemically reactive flows with variable dissipation processes and, hence, are applicable to many fields of science and engineering, such as aerodynamics and combustion simulations.

The time step set for the stability of convection and reaction processes also guarantees stability and convergence of the dissipation processes under normal conditions. Although the total variation is always guaranteed by the inclusion of physical dissipation processes, the stability could collapse with stiff heat conduction. However, this numerical stiffness is irrelevant in the real physical world. The explicit FCT and ADE methods were applied to an inviscid flow, a strong dissipative flow, and a combined reactive, convective, and dissipative flow with physically understandable results.

The elapsed CPU time on a Dec Alpha 2000/300 is approximately 14 h to simulate 24 h of physical time, using our standard time step increment of 50 ms.

Our further work is to apply the FCT-ADE model to both low-latitude and high-latitude thermal plasma transport problems, so that the validity of the model results can be tested by comparing with more accurate measurements. The role of the FCT technique may become particularly important when we model the high-latitude thermal plasma transport, where the flows are often supersonic. Further concern is to look into a way of utilizing part or all of the numerical dissipations introduced in the FCT technique to replace part of the desired physical dissipations. This may lead to a capability of the FCT technique to handle both Eulerian and Navier–Stokes systems as a whole.

ACKNOWLEDGMENTS

One of us, Liqun Zhou acknowledges the valuable discussions with Elaine Oran. We thank the Air Force Office of Scientific Research (AFOSR), Grant F49620-93-1-0010DEF, the Atmospheric Science Division of the National Science Foundation (NSF), Grants ATM-9202820, ATM-9612638, ATM-9302354, and NASA, Grant NAG5-1484, for making the research possible. We also thank T.-Z. Ma for carefully reviewing the numerical aspects of our model.

REFERENCES

1. J. P. Boris and D. L. Book, *J. Comput. Phys.* **11**, 38 (1973).
2. R. W. Schunk, *Rev. Geophys. Space Phys.* **15**, 429 (1977).
3. C. E. Rasmussen and R. W. Schunk, *J. Geophys. Res.* **93**, 14557 (1988).
4. R. W. Schunk and J. J. Sojka, *J. Geophys. Res.* **94**, 8973 (1989).
5. A. Korosmezey, C. E. Rasmussen, T. I. Gombosi, and B. Van Leer, *J. Comput. Phys.* **109**, 16 (1993).
6. H. Z. Barakat and J. A. Clark, *J. Heat Transfer.* **87**, 421 (1966).
7. R. W. Schunk, *PAGEOPH (Switzerland)* **127**, 255 (1988).
8. G. J. Bailey and R. Sellek, *Ann. Geophys.* **8**, 171 (1990).
9. R. J. LeVeque, *Numerical Methods for Conservation Laws* (Birkhäuser, Basel, 1992).
10. R. Warming and B. Hyett, *J. Comput. Phys.* **14**, 159 (1974).
11. J. P. Boris, A. M. Landsberg, E. S. Oran, and J. H. Gardner, NRL Memorandum Report 6410-93-7192, Washington, DC, 1993.
12. J. P. Boris and D. L. Book, *Methods Comput. Phys.* **16**, 85 (1976).
13. S. T. Zalesak, *J. Comput. Phys.* **31**, 335 (1979).
14. E. E. Kunhardt and C. Wu, *J. Comput. Phys.* **68**, 127 (1987).
15. G. Patnaik, K. J. Laskey, K. Kailasanath, E. S. Oran, and T. A. Brunt, NRL Memorandum Report 6555, Washington, DC, 1989.
16. E. S. Oran and J. P. Boris, *Numerical Simulation of Reactive Flow* (Elsevier, New York, 1987).
17. R. J. LeVeque and H. C. Yee, *J. Comput. Phys.* **86**, 187 (1990).
18. V. B. Wickwar, L. Zhou, R. W. Schunk, C. Lathuillere, and J. Lilensten, *J. Geophys. Res.*, in preparation.